7

Variational P-Vector Method

The P-vector inverse method described in chaps. 5 and 6 is to determine the absolute velocity for each water column independently (local determination). This method is simple and straight forward. However, local determination of the absolute velocity field might not guarantee global mass conservation. The variational P-vector method is developed for solving this problem.

7.1 Weakness of the P-Vector Method

Let$(u^{(\mathrm{P})}, v^{(\mathrm{P})})$ be the absolute velocity determined by the P-vector method, and $(U^{(\mathrm{P})}, V^{(\mathrm{P})})$ be their vertical integrations (i.e., volume transport),

$$(U^{(\mathrm{P})}, V^{(\mathrm{P})}) = \int_{-H}^{0} (u^{(\mathrm{P})}, v^{(\mathrm{P})}) \mathrm{d}z. \tag{7.1}$$

Due to the local determination of the absolute velocity, the current P-vector method does not always guarantee the mass conservation over a domain Ω, i.e.,

$$\iint_{\Omega} \left[\frac{\partial U^{\mathrm{P}}}{\partial x} + \frac{\partial V^{\mathrm{P}}}{\partial y} \right] \mathrm{d}x \, \mathrm{d}y \neq 0 \tag{7.2}$$

may happen. Such a deficiency largely affects the quality of the inversion. For example, the Tsushima Warm Current in the shallow Tsushima/Korea Strait was not well-inverted (see Fig. 6.24). Thus, a variational algorithm is used to make the left-hand side of (7.2) close to zero as possible.

7.2 Variational Algorithm

Let (U, V) be the vertically integrated velocity optically determined by minimizing the following functional (called the cost function),

$$J(U,V) = \frac{1}{2}\iint\limits_{\Omega} \left[(U - U^{((\mathrm{P}))})^2 + (V - V^{((\mathrm{P}))})^2\right] \mathrm{d}x\,\mathrm{d}y, \tag{7.3}$$

with the constraint (mass conservation)

$$\frac{\partial U}{\partial x} + \frac{\partial V}{\partial y} = 0$$

This problem becomes an unconstrained optimization using

$$L(U,V,\lambda) = J(U,V) + \iint\limits_{\Omega} \lambda \left[\frac{\partial U}{\partial x} + \frac{\partial V}{\partial y}\right] \mathrm{d}x\,\mathrm{d}y, \tag{7.4}$$

where λ is the Lagrangian parameter.

Let the dependent variable be defined on the interval, $0 \le x \le L_x, 0 \le y \le L_y$. Use a uniform grid,

$$0 = x_1 < x_2 < \ldots < x_{N_x} = L_x, 0 = y_1 < y_2 < \ldots < y_{N_y} = L_y \tag{7.5a}$$

with grid spacing of $(\Delta x, \Delta y\ )$, as shown in Fig. 7.1a. Here, N_x and N_y are numbers of grid points in x and y directions, and

$$\Delta x = x_{i+1} - x_i = L_x/N_x, \quad \Delta y = y_{j+1} - y_j = L_y/N_y. \tag{7.5b}$$

Let ρ, λ be evaluated at the grid point (i,j), and the integrated velocity components $U, V, U^{(\mathrm{P})}, \mathrm{V}^{(\mathrm{P})}$ be evaluated at the staggered points, respectively (Fig. 7.1b). The functional (8.4) is discretized by

$$\begin{aligned}\hat{L} = {} & \frac{1}{2}\sum_{i=1}^{Nx-1}\sum_{j=1}^{Ny-1}\left[(U_{ij} - U_{ij}^{(P)})^2 + (V_{ij} - V_{ij}^{(P)})^2\right]\Delta x\,\Delta y \\ & + \frac{1}{2}\sum_{i=1}^{Nx-1}\sum_{j=1}^{Ny-1}\lambda_{ij}\,(U_{ij} + U_{i,j-1} - U_{i-1,j} - U_{i-1,j-1})\,\Delta y \\ & + \frac{1}{2}\sum_{i=1}^{Nx-1}\sum_{j=1}^{Ny-1}\lambda_{ij}\,(V_{ij} + V_{i,j-1} - V_{i-1,j} - V_{i-1,j-1})\,\Delta x. \end{aligned} \tag{7.6}$$

7.3 Combined Local-Global Determination

Minimization of $\hat{L}$ is a combination of local determination at the staggered grid (i,j) for velocity

$$U_{ij} \to U_{ij}^{(\mathrm{P})}, \quad V_{ij} \to V_{ij}^{(\mathrm{P})}, \tag{7.7}$$

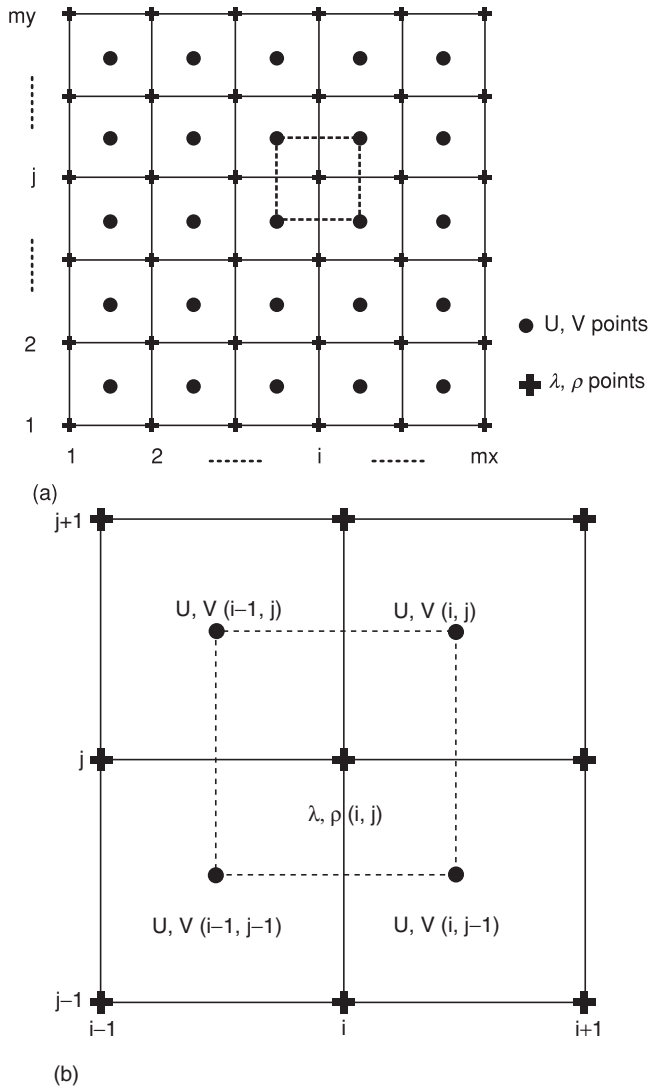

Fig. 7.1. Staggered grid used for the computation: (**a**) grid distribution and (**b**) staggered grids for (u, v) and standard grids for (ρ, λ) (from Chu et al. 2001b, Journal of Physical Oceanography)

and global determination (box model)

$$\frac{1}{\Delta x}\left(U_{ij}+U_{i,j-1}-U_{i-1,j}-U_{i-1,j-1}\right)$$

$$+\frac{1}{\Delta y}\left(V_{ij}+V_{i,j-1}-V_{i-1,j}-V_{i-1,j-1}\right)\rightarrow 0, \tag{7.8}$$

leads to the mass conservation at any box centered at the nonstaggered grid for ρ and λ (Fig. 7.1b). Thus, this variational P-vector method can be treated as a P-vector box model. The variational problem is the determination of $(U_{ij}, V_{ij}, \lambda_{ij})$ through minimizing the cost function

$$\frac{\partial \hat{L}}{\partial U_{ij}} = 0, \quad \frac{\partial \hat{L}}{\partial V_{ij}} = 0, \quad \frac{\partial \hat{L}}{\partial \lambda_{ij}} = 0. \tag{7.9}$$

Substituting(7.6) into (7.9) yields

$$U_{ij} = U_{ij}^{\mathrm{P}} - \frac{1}{2\Delta x}\left(\lambda_{ij} + \lambda_{i,j+1} - \lambda_{i+1,j} - \lambda_{i+1,j+1}\right), \tag{7.10}$$

$$V_{ij} = V_{ij}^{\mathrm{P}} - \frac{1}{2\Delta y}\left(\lambda_{ij} + \lambda_{i,j+1} - \lambda_{i+1,j} - \lambda_{i+1,j+1}\right), \tag{7.11}$$

$$\begin{aligned} &\frac{1}{\Delta x}\left(U_{ij} + U_{i,j-1} - U_{i-1,j} - U_{i-1,j-1}\right) \\ &+ \frac{1}{\Delta y}\left(V_{ij} + V_{i,j-1} - V_{i-1,j} - V_{i-1,j-1}\right) = 0. \end{aligned} \tag{7.12}$$

Substituting (7.10) and (7.11) into (7.12) yields a linear algebraic equation for the Lagrange parameter,

$$\begin{aligned} &a_{11}\lambda_{i-1,j-1} + a_{21}\lambda_{i,j-1} + a_{31}\lambda_{i+1,j-1} + a_{12}\lambda_{i-1,j} + a_{22}\lambda_{i,j} + a_{32}\lambda_{i+1,j} \\ &+ a_{13}\lambda_{i-1,j+1} + a_{23}\lambda_{i,j+1} + a_{33}\lambda_{i+1,j+1} = S_{ij}, \end{aligned} \tag{7.13}$$

where $i = 2, 3, \ldots, N_x - 1, j = 2, 3, \ldots, N_y - 1$, and

$$\begin{aligned} &a_{11} = a_{12} = a_{31} = a_{33} = -\frac{1}{4}\left(\frac{1}{\Delta x^2} + \frac{1}{\Delta y^2}\right), \quad a_{22} = \frac{1}{2}\left(\frac{1}{\Delta x^2} + \frac{1}{\Delta y^2}\right), \\ &a_{21} = a_{23} = -a_{12} = -a_{32} = \frac{1}{2}\left(\frac{1}{\Delta x^2} - \frac{1}{\Delta y^2}\right), \end{aligned} \tag{7.14}$$

and

$$\begin{aligned} S_{ij} = &\frac{1}{2\Delta x}\left(U_{ij}^{(\mathrm{P})} + U_{i,j+1}^{(\mathrm{P})} - U_{i-1,j}^{(\mathrm{P})} - U_{i+1,j+1}^{(\mathrm{P})}\right) \\ &+ \frac{1}{2\Delta y}\left(V_{ij}^{(\mathrm{P})} + V_{i,j+1}^{(\mathrm{P})} - V_{i-1,j}^{(\mathrm{P})} - V_{i+1,j+1}^{(\mathrm{P})}\right). \end{aligned} \tag{7.15}$$

The alternative-direction implicit (ADI) method (Press et al. 1986) is used to obtain the value of the Lagrange parameter at the grid point, λ_{ij} solving

(7.13). Substituting the given value of λ_{ij} into (7.10) and (7.11) yield the optimal estimation of U_{ij} and V_{ij}.

After the vertically integrated velocity (U, V) is calculated, the bottom velocity can be determined. Let $h = h(x, y)$ be the bottom topography and (u_{-h}, v_{-h}) be the bottom velocity. Applying the thermal wind relations (1.4) and (1.5) to the two levels z and $-h$, we have

$$(u, v)_z - (u, v)_{-h} = \frac{g}{f\rho_0} \int_{-h}^{z} \left(\frac{\partial \rho}{\partial y}, -\frac{\partial \rho}{\partial x} \right) \mathrm{d}z'. \tag{7.16}$$

Vertical integration of (7.16) from the bottom ($z = -h$) to the surface ($z = 0$) yields

$$(u, v)_{-h} = \frac{1}{h}(U, V) - \frac{g}{fh\rho_0} \int_{-h}^{0} \mathrm{d}z \int_{-h}^{z} \left(\frac{\partial \rho}{\partial y}, -\frac{\partial \rho}{\partial x} \right) \mathrm{d}z'. \tag{7.17}$$

With the computed bottom velocity $(u, v)_{-h}$, we use the thermal wind relations (1.4) and (1.5) to obtain the absolute velocity from the density field.

7.4 Annual Mean Velocity

Figure 7.2 shows the inverted horizontal velocity vectors at 0-, 50-, 100-, 150-, 200-, and 300-m deep, respectively. The variational P-vector method inverts the velocity well at the three major straits: Tsushima/Korea, Tsugaru, and Soya Straits. However, the flow in Tatar Strait is not well resolved due to the poor data quality.

We take the velocity field at 0-, 50-, and 100-m (150-, 200-, and 300-m) deep to represent the upper (intermediate) layer circulation features. The inverted velocity field agrees well with early results using the ordinary P-vector method (see Sect. 6.5.5) except for flow in the straits which is more improved.

7.4.1 Upper Layer

The most striking feature of the upper layer circulation is its three-branch structure. North of 35°N, the Tsushima Warm Current bifurcates into an eastern portion (the first branch, or the Japan Near-Shore Branch) and a western portion. The strength of the Tsushima Warm Current at both portions reduces with depth. Flow through the western portion (i.e., East Korean Warm Current) closely follows the Korean Coast until it separates near $37° - 38°$N into two branches: the off-shore branch (the second branch, i.e., the Polar Front Current) follows the Polar Front to the western coast of Hokkaido Island, and the along-shore branch (or the third branch) moves northward (i.e.,

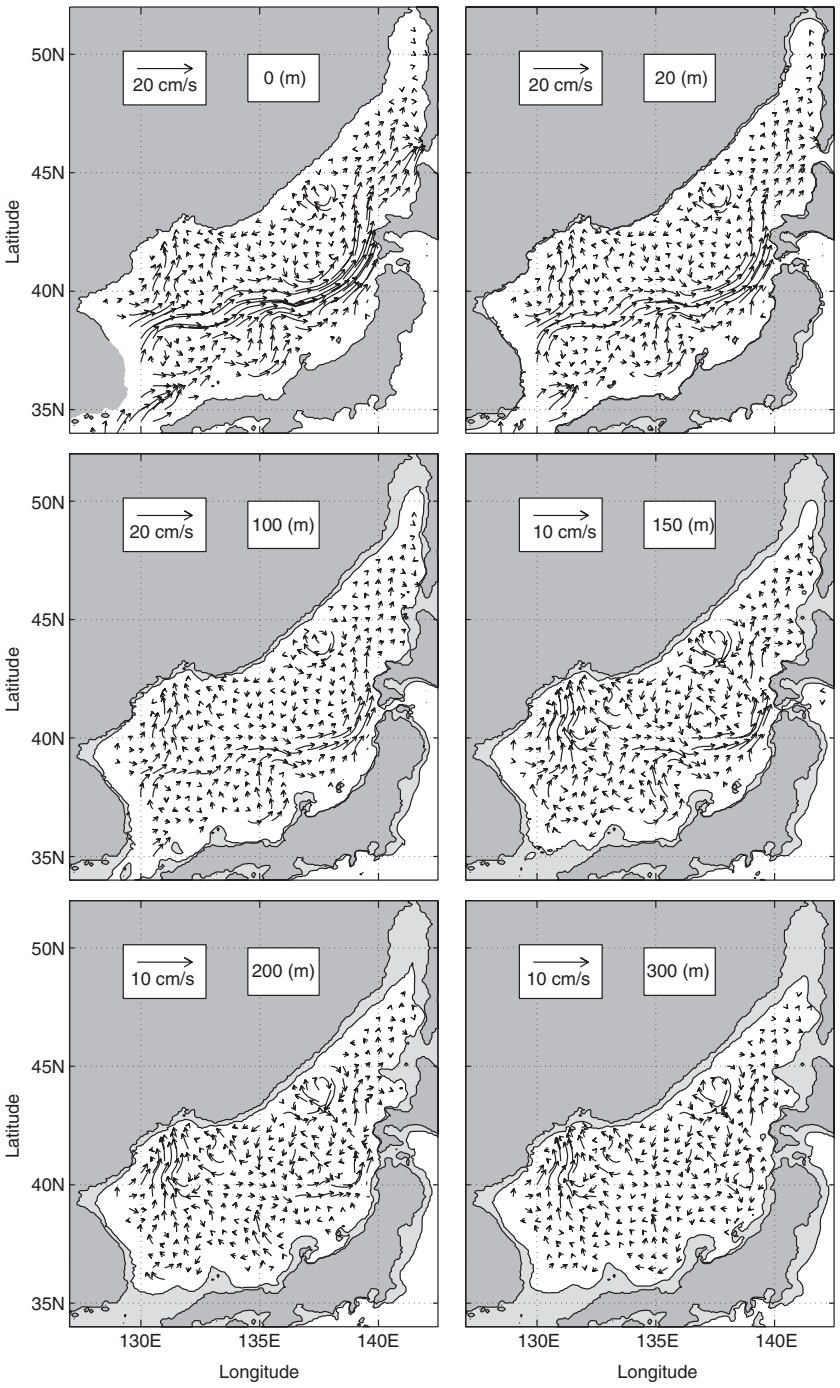

Fig. 7.2. Inverted annual mean horizontal velocity vectors at different depths: (**a**) 0 m, (**b**) 50 m, (**c**) 100 m,(**d**) 150 m, (**e**) 200 m, and (**f**) 300 m (from Chu et al. 2001b, Journal of Physical Oceanography)

the East Korean Warm Current). Such a three-branch pattern was first identified by Suda and Hidaka (1932) and Suda et al. (1932) using hydrographic and current meter data from June to September in 1929 and in 1930, respectively. Since then, the existence of three branches has been believed to be the typical Tsushima Warm Current flow pattern. The second branch (i.e., the Polar Front Current) is stronger than the first branch (i.e., the Japan Near-Shore Branch).

The maximum speed of the Polar Front Current is found around $0.2\,\mathrm{m\,s^{-1}}$ at the surface. The maximum speed of the Japan Near-Shore Branch is found to be around $0.1\,\mathrm{m\,s^{-1}}$, occurring near the Japanese coast (135°E–35.5°N) at the surface. The second feature of the upper layer circulation is its multieddy structure. An evident cyclonic gyre is identified in the Japan Basin (135°–140°E, 38°–44°N) with the flow associating with the Polar Front Current as its southern and eastern flanks and the flow from the north as its western flank. A mesoscale anticyclonic eddy is identified in the Ulleng/Tsushima Basin (130°–132°E, 36°–38°N) with the Polar Front Current as its northern and western flanks. The velocity field weakens with depth.

7.4.2 Intermediate Layer

The most striking feature of the intermediate layer circulation is its multieddy structure. The Polar Front Current weakens at 150 m deep and disappears at 200 and 300 m depth. The cyclonic gyre in the Japan Basin (135°–140°E, 38°–44°N) is evident with a maximum speed to be around $0.1\,\mathrm{m\,s^{-1}}$. The Ulleng/Tsushima Basin anticyclonic eddy is evident at 150 and 200 m depth and weakens drastically at 300 m depth.

7.5 Seasonal Variability

The seasonal variability of the inverted absolute velocity (not in the straits) is quite similar to an early study using the ordinary P-vector method (see Sect. 6.5.5).

7.5.1 Surface Circulation

The velocity variability reduces with depth since the seasonal density variability weakens with depth. The Polar Front Current has a weak seasonal variation in flow pattern and a strong seasonal variation in current speed. The Japan Near-Shore Branch is too weak to be identified in winter (December–February). In March, it starts to occur along the Japan coast, and strengthens in spring and reaches the maximum velocity in July.

An interesting feature in the surface currents (Fig. 7.3) is the out-of-phase variation between Polar Front Current (along the Polar Front) and Japan Near-Shore Branch (along the west coast of Japan). For example, the Polar

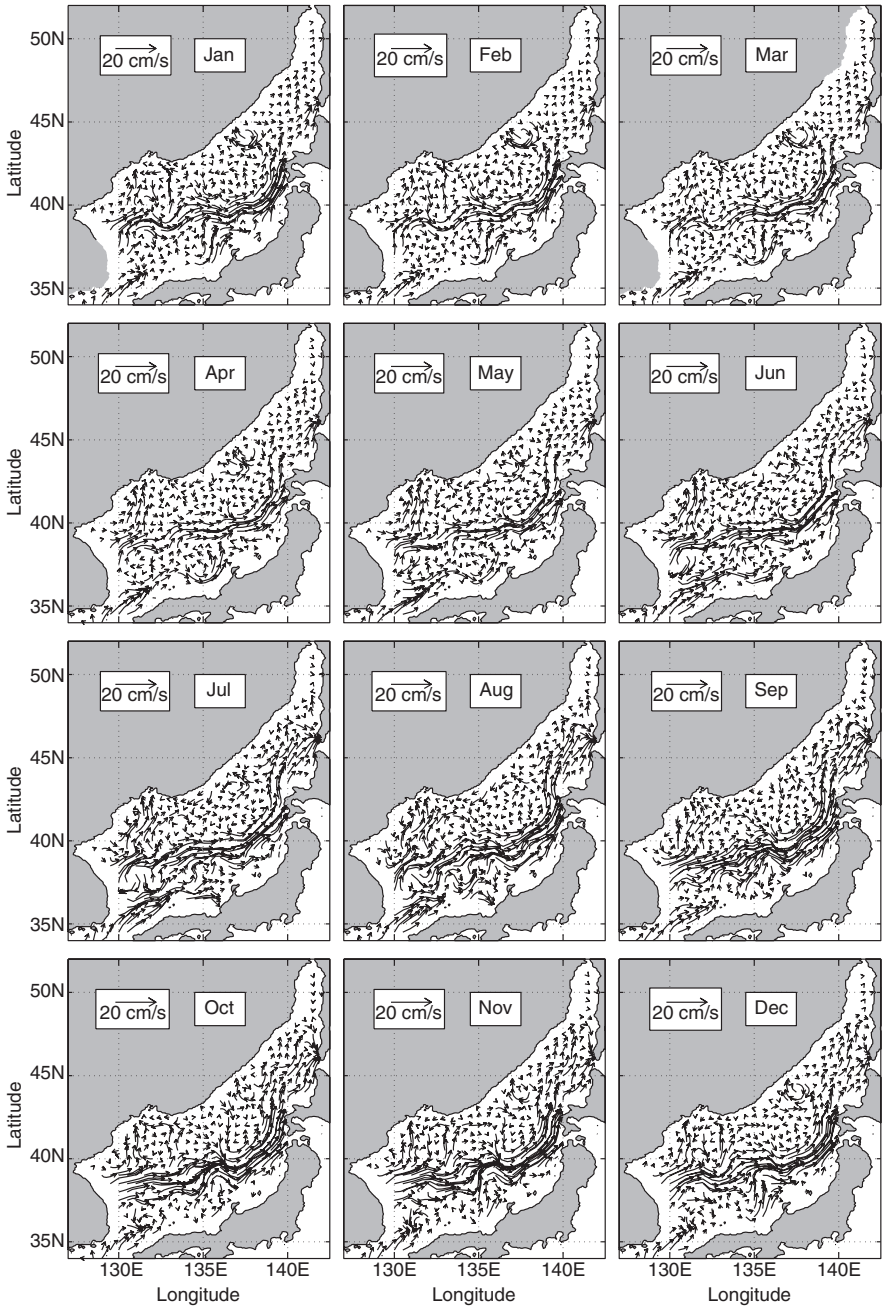

Fig. 7.3. Inverted monthly mean surface horizontal velocity vectors (from Chu et al. 2001b, Journal of Physical Oceanography)

Front Current (Japan Near-Shore Branch) strengthens (weakens) from July to September, and weakens (strengthens) from January to April.

The Japan Basin cyclonic gyre occurs all the year round with the flow associated with the Polar Front Current as the southern and eastern flanks and the flow from the north as the western flank. The seasonal variability of this gyre is largely determined by the seasonal variability of the Polar Front Current.

7.5.2 Out-of-Phase Variation

The seasonal variation of the Japan/East Sea major currents is also shown in the meridional cross-section (135°E) of the monthly mean u-component (7.4). Two eastward flowing currents, the Polar Front Current (38°–40°N) and Japan Near-Shore Branch (36°–37°N), are well represented. The Polar Front Current is strong from September to December with the maximum speed of $0.2\,\mathrm{m\,s^{-1}}$ and weak from February to June with a minimum speed of $0.1\,\mathrm{m\,s^{-1}}$. During the summer monsoon season (June–October), the Polar Front Current strengthens (maximum speed increases from 0.12 to $0.18\,\mathrm{m\,s^{-1}}$), and the Japan Near-Shore Branch weakens (maximum speed decreases from 0.12 to $0.04\,\mathrm{m\,s^{-1}}$) During the winter monsoon season (December–April), the Polar Front Current weakens (maximum speed decreases from 0.18 to $0.12\,\mathrm{m\,s^{-1}}$), and the Japan Near-Shore Branch strengthens (maximum speed increases from 0.04 to $0.12\,\mathrm{m\,s^{-1}}$).

7.5.3 Ulleung/Tsushima Basin Anticyclonic Eddy

The seasonal variation of the Ulleng/Tsushima Basin anticyclonic eddy is shown in the zonal cross-section (37°N) of monthly mean v-component (Fig. 7.5) between 130°E and 132°E: the northward flow in the west and the southward flow in the east. The inverted Ulleng/Tsushima Basin eddy has a core from the surface to 100 m deep with a maximum swirl velocity of $0.06\,\mathrm{m\,s^{-1}}$. It is quite evident during the whole winter season (December–February) and weakens in March. It cannot be identified at the 37°E cross-section from spring to early summer (April–June) and becomes evident again in late summer (August).

7.5.4 Flow through Tsushima/Korea Strait

The monthly mean surface velocity vector field in Tsushima/Korea Strait (Fig. 7.6) shows the capability of the variational P-vector method to invert the currents in shallow straits. The inverted general circulation pattern agrees with the observational circulation pattern using Acoustic Doppler Current Profiler (ADCP) reported by Egawa et al. (1993): The main axis of the Tsushima Warm Current exists in the western channel at 34°N for all months, and the current in the eastern channel is relatively weak. The seasonal variation of the current magnitude is quite small. Northeastward steady flow always exists in the middle of the strait with a maximum current speed of $0.1\,\mathrm{m\,s^{-1}}$.

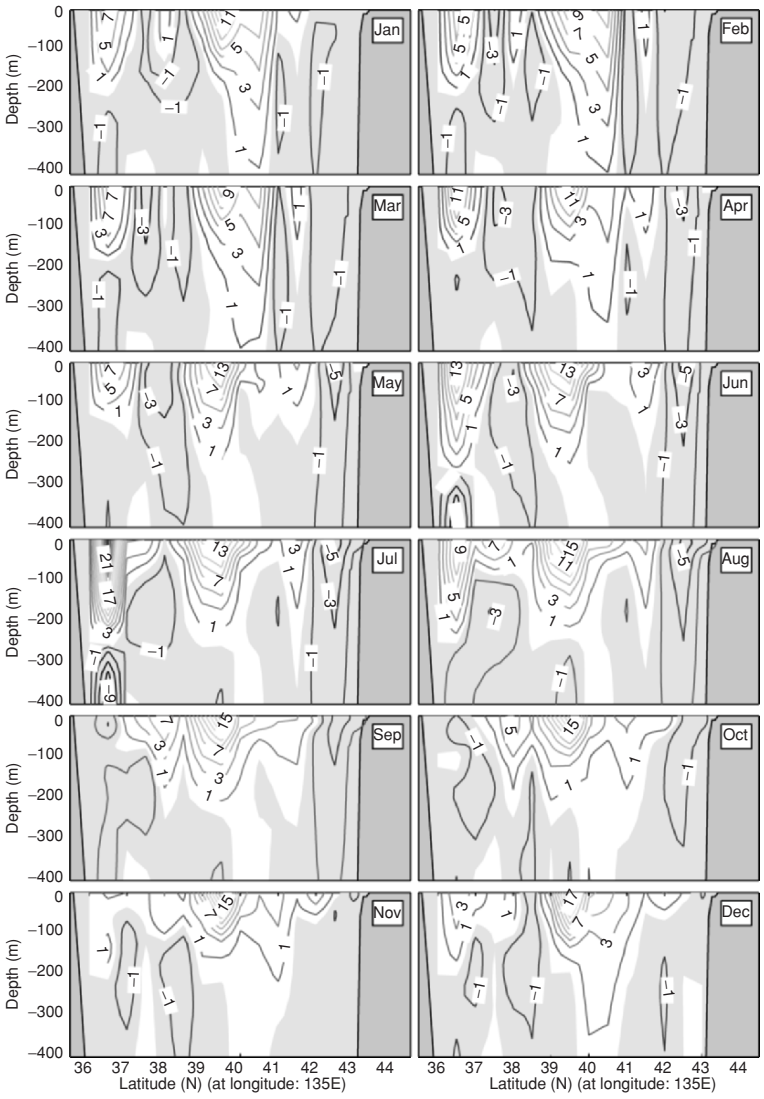

Fig. 7.4. Meridional cross-sections of the inverted monthly mean u velocity (unit: $10^{-2}\,\mathrm{m\,s^{-1}}$) along 135°E (from Chu et al. 2001b, Journal of Physical Oceanography)

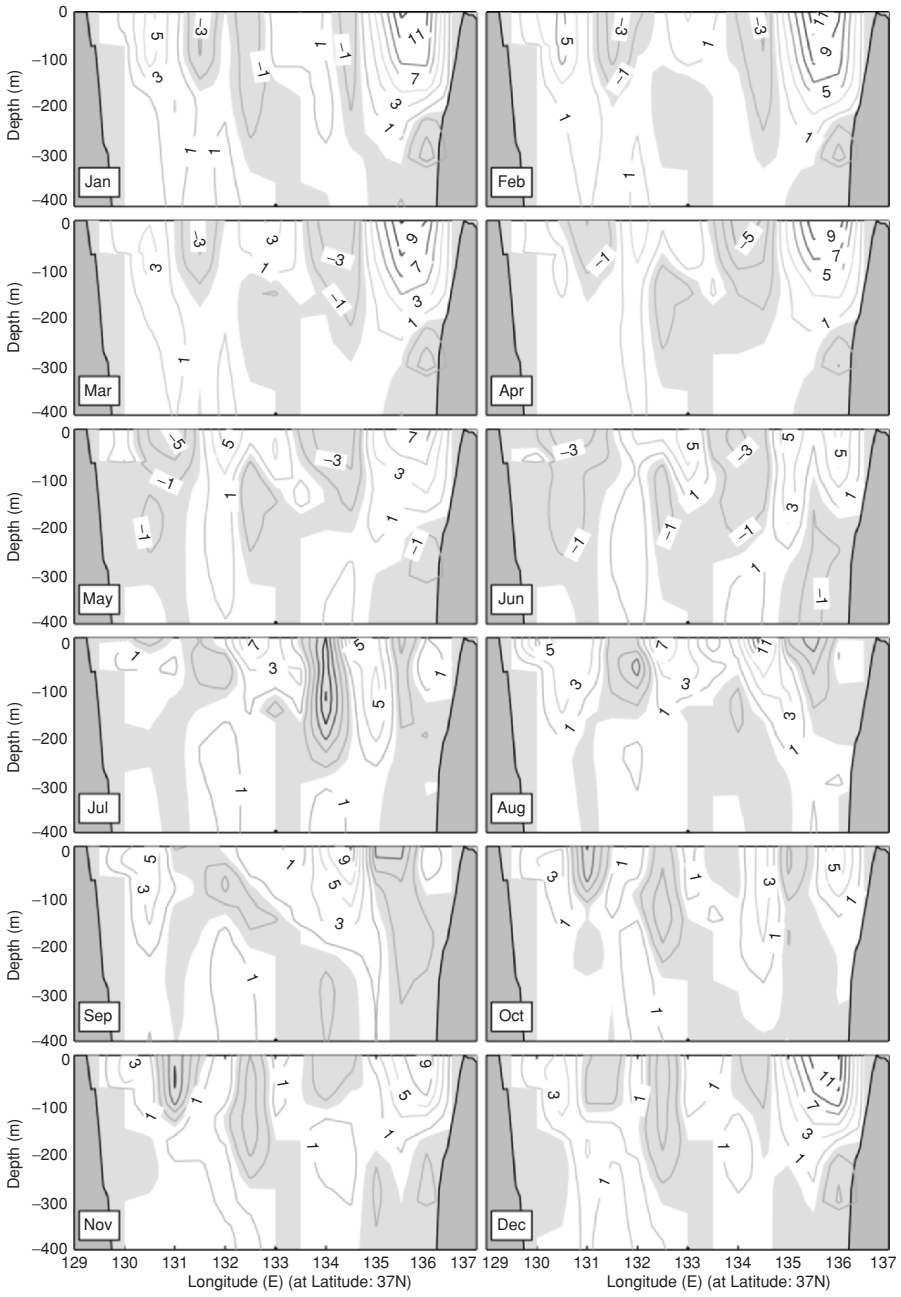

Fig. 7.5. Zonal cross-sections of inverted monthly mean v velocity (unit: $10^{-2}\,\mathrm{m\,s^{-2}}$) along 37°N (from Chu et al. 2001b, Journal of Physical Oceanography)

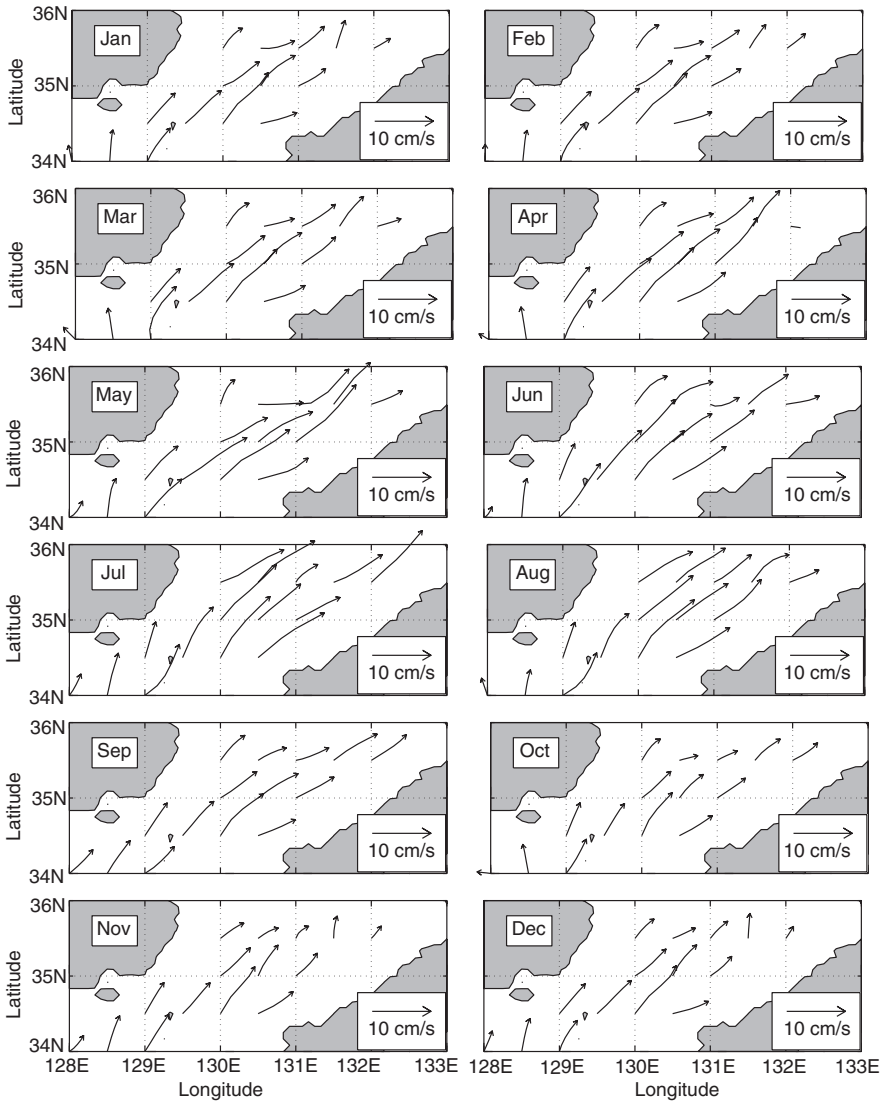

Fig. 7.6. Inverted monthly mean surface horizontal velocity vectors in the Tsushima/Korean Strait (from Chu et al. 2001b, Journal of Physical Oceanography)

7.6 Volume Transport Through Tsushima/Korea, Tsugaru, and Soya Straits

Warm water enters the Japan Sea through the Tsushima/Korea Strait with the Tsushima Warm Current from the East China Sea and exits the Japan Sea through the Tsugaru and Soya straits. An evident volume transport through Tatar Strait is not found (Martin and Kawase 1998). Using the inverted absolute velocity field, we calculate the monthly mean volume transport through the four straits. The transport through Tatar Strait is zero. The transports through Tsushima/Korea, Tsugaru, and Soya Straits are shown in Fig. 7.7. An evident seasonal variation is found in Tsushima/Korea Strait with a minimum value of 1.9 Sv in November and a maximum value of 2.9 Sv in July (Table 7.1). The annual mean volume transport is 2.3 Sv, and the range (maximum minus minimum) of the seasonal variation is 1.0 Sv. This range (1.0 Sv) is larger than Isobe's (1994) estimation (0.7 Sv) using the sea level difference across the strait, smaller than Inoue et al.'s (1985) estimation (1.61 Sv) with 3.43 Sv in summer and 1.82 Sv in winter, and Yi's (1966) estimation (1.9 Sv) with a maximum of 2.2 Sv in October and a minimum of 0.3 Sv in February.

The volume transport in Soya Strait (outflow) has a similar seasonal variation to that in Tsushima/Korea Strait. The maximum (minimum) outflow from Soya Strait is 1.4 Sv (0.5 Sv) in July (December). The annual range is 0.9 Sv. The volume transport in Tsugaru Strait (outflow) has a rather weak seasonal variability. The maximum (minimum) outflow from Tsugaru Strait is 1.6 Sv (1.2 Sv) in December (September). The annual range is 0.4 Sv. The ratio of the outflow through Tsugaru vs. Soya Strait varies from a maximum value of 3.2 in December to a minimum value of 1.1 in July. The inverted circulation pattern agrees well with the numerical modeling results (Chu et al. 2000c, 2003c).

The inverted inflow transport through Tsushima/Korea Strait equals the total outflow transport through Tsugaru and Soya Straits (a mass-conservation pattern, see Table 7.1). Such a feature indicates the improvement of the variational P-vector method over the original P-vector method, and might be practically useful in determining open boundary conditions for regional numerical models. For example, some Japan Sea circulation models use constant outflow partitioning: Chu et al. (2001b) (or Bang et al. 1996) assumed that 75% (80%) of the total inflow transport flows out of the Japan Sea through Tsugaru Strait, and 25% (20%) through Soya Strait. Such an uncertainty in the open boundary conditions can be eliminated when the variational P-vector method is used.

The variational P-vector method is a combined box/P-vector model. It has the capability to invert the Japan Sea circulation reasonably well and in particular at the three major straits: Tsushima/Korea, Tsugaru, and Soya Straits. The inverted absolute velocity field coincides with earlier observational depiction of the Japan/East Sea circulation.

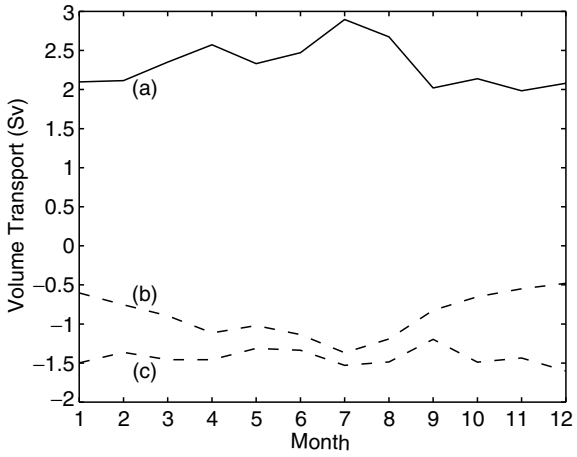

Fig. 7.7. Inverted monthly mean surface horizontal velocity vectors in the Tsushima/Korean Strait (from Chu et al. 2001b, Journal of Physical Oceanography)

Table 7.1. Inverted monthly variation of volume transport (Sv) at the three major straits. The positive/negative values mean inflow/outflow (from Chu et al. 2001b, Journal of Physical Oceanography)

	Jan	Feb	Mar	Apr	May	Jun	Jul	Aug	Sep	Oct	Nov	Dec
soya	0.6	0.7	0.9	1.1	−1.0	−1.1	−1.4	−1.2	−0.8	−0.7	0.5	−0.5
tsugaru	1.5	1.4	1.5	1.5	−1.3	−1.3	−1.5	−1.5	−1.2	−1.5	−1.4	−1.6
tsushima	2.1	2.1	2.4	2.6	2.3	2.4	2.9	2.7	2.0	2.2	1.9	2.1

Questions and Exercises

(1) What is the major weakness of the P-vector inverse method? Why?
(2) The variational P-vector method is to minimize

$$L(U,V,\lambda) = J(U,V) + \iint\limits_{\Omega} \lambda \left[\frac{\partial U}{\partial x} + \frac{\partial V}{\partial y}\right] \mathrm{d}x\,\mathrm{d}y, \tag{E7.1}$$

where λ is the Lagrangian parameter. What conditions do you get from $\partial L/\partial U = 0$, $\partial L/\partial V = 0$, or $\partial L/\partial \lambda$=0?
(3) What improvement can you identify from the comparison between Fig. 7.3 and Fig. 6.24 when the variational scheme is used for the P-vector method?
(4) What are the major features of the Japan/East Sea multieddy structure?

(5) Discuss the current features and transports at the Tsushima/Korean Strait from Figs. 7.6 and 7.7
(6) The volume transports at the three major straits of the Japan/East Sea (Soya, Tsugura, and Tsushima/Korean) are calculated using the variational P-vector method as shown in Table 7.1. Search the literature to find agreement and disagreement with other authors.